Chapter 2
Pulse-Width Modulation

Jian Sun

2.1 Form and Function

Pulse-width modulation (PWM) is the basis for control in power electronics. The theoretically zero rise and fall time of an ideal PWM waveform represents a preferred way of driving modern semiconductor power devices. With the exception of some resonant converters, the vast majority of power electronic circuits are controlled by PWM signals of various forms. The rapid rising and falling edges ensure that the semiconductor power devices are turned on or turned off as fast as practically possible to minimise the switching transition time and the associated switching losses. Although other considerations, such as parasitic ringing and electromagnetic interference (EMI) emission, may impose an upper limit on the turn-on and turn-off speed in practical situations, the resulting finite rise and fall time can be ignored in the analysis of PWM signals and processes in most cases. Hence only ideal PWM signals with zero rise and fall time will be considered in this chapter.

Pulse-width modulation can take different forms [3]. The pulse frequency is one of the most important parameters when defining a PWM method and can be either constant or variable. A constant-frequency (CF) PWM signal can be produced simply by comparing a reference signal, $r(t)$, with a carrier signal, $c(t)$, as depicted in Fig. 2.1a. The binary PWM output can be mathematically written as

$$b_{\text{pwm}}(t) = \text{sgn}\big[r(t) - c(t)\big], \tag{2.1}$$

where 'sgn' is the sign function.

Three types of carrier signals are commonly used in constant-frequency PWM:

1. Sawtooth Carrier, reported in Fig. 2.1b: The leading (rising) edge of PWM output occurs at fixed instants in time while the position of the trailing (falling) edge is

J. Sun (✉)
Department of Electrical, Computer, and Systems Engineering, Rensselaer Polytechnic Institute, Troy, NY 12180-3590, USA
e-mail: jsun@rpi.edu

F. Vasca, L. Iannelli (eds.), *Dynamics and Control of Switched Electronic Systems*, Advances in Industrial Control,
DOI 10.1007/978-1-4471-2885-4_2,

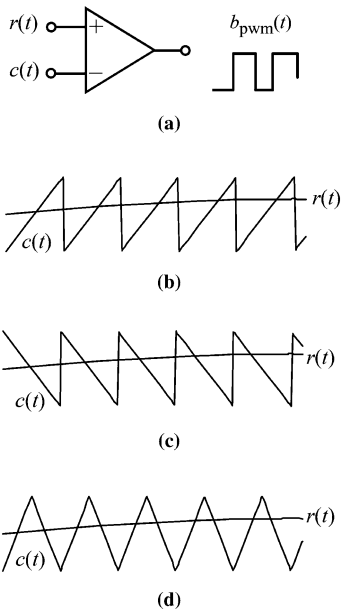

Fig. 2.1 Constant-frequency PWM implemented by a comparator with different carrier signals

modulated as the reference signal level varies. Hence the method is also called constant-frequency *trailing-edge modulation*.

2. Inverted Sawtooth Carrier, reported in Fig. 2.1c: The trailing (falling) edge of PWM output occurs at fixed instants in time while the position of the leading (rising) edge is modulated as the reference signal level varies. The method is usually referred to as constant-frequency *leading-edge modulation*.
3. Triangle Carrier, reported in Fig. 2.1d: Both the leading edge and the trailing edge of the PWM output is modulated. The rising and falling edge of the triangle are usually symmetric so that the pulse is centred within a carrier cycle when the reference is a constant. The method is called constant-frequency *double-edge modulation*.

Trailing-edge modulation is most common in DC–DC converters. As will be discussed in the next section, double-edge modulation eliminates certain harmonics when the reference is a sine wave, and is a preferred method for AC–DC and DC–AC converters where the PWM reference contains a sinusoidal component. A combination of synchronised leading-edge and trailing-edge modulation has also been used to control a boost single-phase power factor correction (PFC) converter and a buck DC–DC converter to reduce ripple in the intermediate DC bus capacitor [25].

The illustrations in Fig. 2.1 assumed analog implementation. When digital implementation is used, the reference is usually sampled at a regular frequency and the carrier can be replaced by a counter/timer. To avoid multiple switching transition within a carrier cycle, the reference should be sampled at the point where the carrier reaches its peak or valley [9]. Pulse-width modulation using such sampled references is called *regular-sampling* PWM. To distinguish from such sampled PWM,

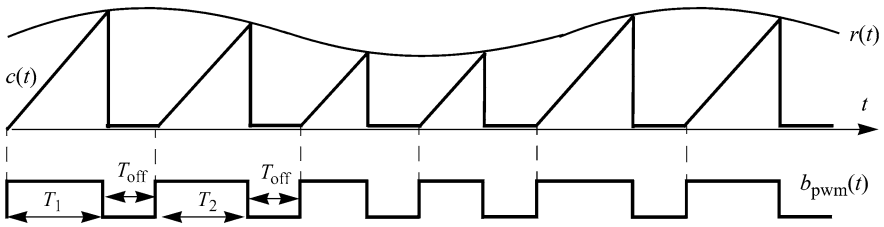

Fig. 2.2 Variable-frequency PWM with constant OFF-time

the analog version discussed before is also called *natural-sampling* PWM in the literature. With a sawtooth or inverted sawtooth carrier, samples are usually taken at the beginning of a carrier cycle. With a triangle carrier, on the other hand, the reference can be sampled either once at the peak of the triangle or twice at both the peak and the valley of the triangle; the former is referred to as *symmetrical sampling*, while the latter is called *asymmetrical sampling* due to the fact that the rising and falling edge of the triangle are compared with different samples of the reference. Regular-sampling PWM is usually used in high power inverters and rectifiers and will not be further discussed in this chapter. On the other hand, the effects of sampling can be incorporated into the PWM spectral models by modifying the double Fourier integral to be presented in the following sections [9].

Variable-frequency (VF) PWM, although not as popular as CF PWM, has also been used in practice. Three common variations of VF PWM are: (a) constant OFF-time, variable ON-time; (b) constant ON-time, variable OFF-time; and (c) hysteretic control. Figure 2.2 depicts constant OFF-time, variable ON-time PWM using a sawtooth-like carrier signal. The switch is turned on after a fixed OFF-time, T_{off}, at which point the sawtooth signal also starts to rise at a constant rate. The switch is turned off again when the sawtooth signal intersects with the reference, at which point the carrier signal is reset to zero. The switch is then kept OFF for a fixed time (T_{off}) again before the next switching cycle starts. As can be seen, the ON-time changes with the reference and the switching frequency increases with the decrease in the reference level, resulting in a variable frequency operation when the reference varies. Constant ON-time, variable OFF-time can be implemented in a similar manner. A popular application of the VF PWM is in boundary-mode control of boost power factor correction (PFC) converters, where the switch operates with a constant ON-time and is turned on as soon as the diode current reduces to zero, resulting in an average input current that is proportional to the input voltage [22]. Hysteretic control is usually applied in conjunction with a current or voltage regulator, and doesn't involve an explicit PWM process. It will not be further discussed in this chapter.

One common concern about VF PWM is the difficulty associated with the design of input and output filters. The filter corner frequency would have to be selected based on the lowest possible switching frequency in order to provide the required attenuation for ripple and EMI under all operation conditions. This usually leads to a conservative design with significant volume and cost penalties. On the other hand, both constant ON-time and constant OFF-time VF PWM exhibit a leading phase

angle in their small-signal dynamic transfer functions, as will be demonstration in Sect. 2.3 of this chapter. Since the modulator is part of the feedback control loop, such a leading phase boosts the phase angle of the loop at high frequencies, thereby improving the stability.

The reference signal depends on the application and is usually independent of the modulation method. For DC–DC converters, the PWM reference is a constant when the converter operates in a steady state but varies whenever the converter goes through a transient. The spectral characteristics of such a PWM waveform with constant frequency and constant duty ratio can be readily determined by Fourier analysis. To characterise the dynamic behaviour of a modulator in DC–DC converters, the reference can be assumed to consist of a DC value corresponding to the steady-state duty ratio and a sinusoidal component representing a small-signal perturbation. A small-signal model can be obtained for the modulator by computing the component in the PWM output at the frequency of the sinusoidal perturbation. Such small-signal models will be developed in Sect. 2.3 for both constant-frequency and variable-frequency PWM.

For AC–DC and DC–AC converters, the reference signal typically contains at least one sinusoidal component at the fundamental frequency of the AC input or output of the converter. For poly-phase (e.g. three-phase) converters, each phase will have a separate reference and their sinusoidal components are shifted from each other by the same phase angle that separates the input or output phase voltages. Often, the PWM references also contain harmonics of the fundamental component. This is the case, for example, in three-phase converters where triple harmonics can be purposely injected into the PWM references to increase the utilisation of the DC voltage, that is, to maximise the AC voltages that can be produced from a given DC voltage source before the modulator saturates [20].

For the reasons stated above as well as for the purpose of developing general PWM models, the reference signal, $r(t)$, is this chapter is assumed to consist of a DC and a single-frequency sinusoidal component in general:

$$r(t) = R_0 + R_1 \cos(2\pi f_1 t + \theta_1). \tag{2.2}$$

This will be used in the spectral analysis of different PWM methods in the next two sections. Each of the amplitudes R_0 and R_1 can be set to zero depending on the specific applications under study. Additional harmonics can also be included in (2.2) if needed.

Mathematical analysis will be presented for different PWM processes in the following sections to develop a more in-depth understanding of their characteristics and to provide models that can be used for different design purposes. Section 2.2 introduces double Fourier series as a general method to characterise constant-frequency PWM processes. Spectral characteristics of different PWM methods are also compared using the double Fourier series models. Section 2.3 discusses small-signal modelling of both constant-frequency and variable-frequency pulse-width modulator for dynamic modelling and control design of DC–DC converters. The section also studies the effects of interleaved PWM of multiple converter modules and uses the analytical spectral models to characterise the ripple cancellation effects

under different interleaving strategies. Section 2.4 discusses peak current control, a control method widely used in DC–DC converters where the inductor current is used in place of the carrier signal for PWM control.

2.2 PWM Spectral Modelling and Characteristics

This section presents the development of mathematical models for constant-frequency PWM signals where the reference is defined by (2.2). All three types of carrier signals—sawtooth, inverted sawtooth and triangle—will be considered. The objective is to obtain analytical models that describe the PWM output spectrum when each type of carrier signal is used. Such spectral models are especially important for AC–DC and DC–AC converter applications where the PWM spectrum is directly related to the harmonics in the input or output voltage and current of the converter.

A periodic function can be represented by a Fourier series. A PWM waveform is periodic if the carrier frequency, denoted as f_c hereafter, and the fundamental frequency f_1 of the reference defined in (2.2) are commensurable, that is, if the frequency ratio f_c/f_1 is a rational number. In the special case when f_c is a multiple of f_1, Fourier analysis can be performed on the PWM waveform over a period corresponding to one cycle of the reference, that is, a time interval equal to $1/f_1$. However, even in such a special case, carrying out the Fourier analysis is not an easy undertaking because each switching point in the PWM waveform is defined by a trigonometric equation involving both the sinusoidal reference defined by (2.2) and a linear function of time representing the carrier signal. Since such equations can only be solved numerically, the Fourier analysis results will be specific to the case analysed and have to be redeveloped if any parameter involved changes. In the more likely case where the carrier frequency is not a multiple of (but still commensurable with) the reference fundamental frequency, Fourier analysis would have to be performed over an interval corresponding to multiple fundamental cycles, making the numerical problem quickly intractable.

The double Fourier series method introduced below solves this problem by reformulating the mathematics that define the PWM waveform. Instead of the original function of time involving two different frequencies, a new two-dimensional function is introduced where the carrier and the reference fundamental frequency each corresponds to an independent variable. The two-dimensional function is decomposed using a double Fourier series which is then converted back into a function of time involving both frequencies to give the spectrum of the original PWM waveform.

2.2.1 Double Fourier Series Method

Double Fourier analysis is a generalisation of the conventional Fourier analysis to two-dimensional functions. According to mathematical theory [24], a two-

dimensional function $f(x, y)$ that is periodical in both x and y, with a period equal to 2π in both axes, can be represented by a double Fourier series in the form of

$$f(x,y) = \frac{A_{00}}{2} + \sum_{n=1}^{+\infty}(A_{0n}\cos ny + B_{0n}\sin ny) + \sum_{m=1}^{+\infty}(A_{m0}\cos mx + B_{m0}\sin mx) + \sum_{m=1}^{+\infty}\sum_{n=\pm 1}^{\pm\infty}\big(A_{mn}\cos(mx+ny) + B_{mn}\sin(mx+ny)\big), \tag{2.3}$$

where the coefficients are defined as follows:

$$A_{mn} = \frac{1}{2\pi^2}\int_0^{2\pi}\int_0^{2\pi} f(x,y)\cos(mx+ny)\,\mathrm{d}x\,\mathrm{d}y, \tag{2.4}$$

$$B_{mn} = \frac{1}{2\pi^2}\int_0^{2\pi}\int_0^{2\pi} f(x,y)\sin(mx+ny)\,\mathrm{d}x\,\mathrm{d}y. \tag{2.5}$$

Double Fourier series method was first used to model PWM signals in for communication applications [2]. Reference [13] presented spectral models of different PWM signals using this method. Application of the method in power electronics first appeared in [5], and more systematically in [9]. The book [3] by Black provides a detailed explanation of the double Fourier analysis method as applied to constant-frequency trailing-edge PWM. The review below follows the presentation of [3] in order to develop an understanding of the original and elegant idea introduced in [2].

The first step is to reformulate the PWM process such that it can be described by a two-dimensional function. This is illustrated in Fig. 2.3 for constant-frequency trailing-edge modulation. Figure 2.3a shows the sawtooth carrier and the reference signal, and Fig. 2.3b shows the resulting PWM output. Figure 2.3c is generated by stacking multiple carrier and reference sets $\{(c(t), r(t)\}$, $\{C_m + c(t), C_m + r(t)\}$, $\{2C_m + c(t), 2C_m + r(t)\}$, ..., where C_m is the peak-peak amplitude of the carrier signal. Line AB is an extension of the first slope of the original sawtooth signal. The horizontal lines l_1, l_2, ..., separate the stacked carriers and are spaced from each other by C_m. Note that the intersection points of line AB with these lines and the stacked references are the same as those between the original carrier and reference shown in Fig. 2.3a. Hence they define the same PWM waveform. This provides an alternative way to define, mathematically, the trailing-edge PWM process.

A similar representation can be developed for other PWM methods. Figure 2.4 shows how this is done for double-edge modulation using a triangle carrier. Unlike in the case with a sawtooth carrier, an alternate sequence of the original carrier and reference and their inverse are stacked in this case. In other words, the stacked carriers are $c(t)$, $2C_m - c(t)$, $2C_m + c(t)$, $4C_m - c(t)$, ..., and the stacked references are $r(t)$, $2C_m - r(t)$, $2C_m + r(t)$, $4C_m - r(t)$, ... Line AB is an extension of the rising edge of the first triangle of the original carrier, $c(t)$. Note again that the intersection points of line AB with the stacked references are the same as those between the original carrier and reference.

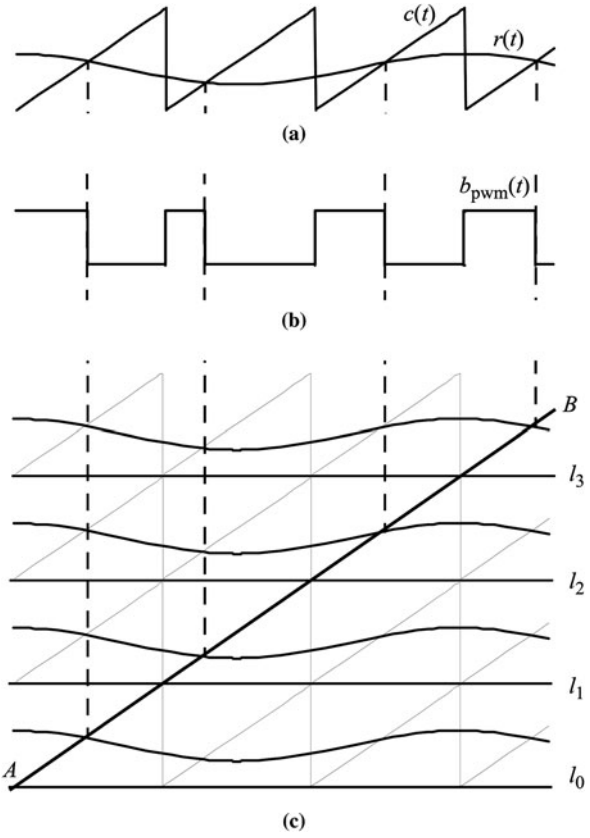

Fig. 2.3 CF trailing-edge modulation and its alternative representation for the development of a double Fourier series

The second step in the development of a double Fourier series representation is to define a two-dimensional function based on the alternative arrangement introduced above. Take double-edge modulation as example. Redefine the horizontal axis in Fig. 2.4c as x axis and let $x = 2\pi f_1 t + \theta_1$. Additionally, redefine the vertical axis as y axis and let $y = 2\pi f_c t + \theta_c$ so that the height of the triangle in the original coordinate system corresponds to π in y. θ_1 and θ_c are the initial phase angle of the reference and the carrier at $t = 0$, respectively. This new x–y coordinate system is illustrated in Fig. 2.5a where the stacked reference waveforms are represented by the edge of the shadowed areas. Imagine now a three-dimensional graph defined by a function $z = f(x, y)$ which is equal to $+1$ when the point (x, y) lies inside any of the shadowed areas, and -1 otherwise, as illustrated in Fig. 2.5b. It is obvious that is periodic in both x and y, with a common period equal to 2π. Therefore, $f(x, y)$ can be represented by a double Fourier series. Note that the double Fourier coefficients are defined analytically and no numerical values are involved up to this point.

Line AB in the x–y–z coordinate system is defined implicitly by $x = 2\pi f_1 t + \theta_1$ and $y = 2\pi f_c t + \theta_c$. Imagine now a vertical plane is erected along the line, indicated by the dashed line in Fig. 2.5b. This plane cuts across the three-dimensional graph

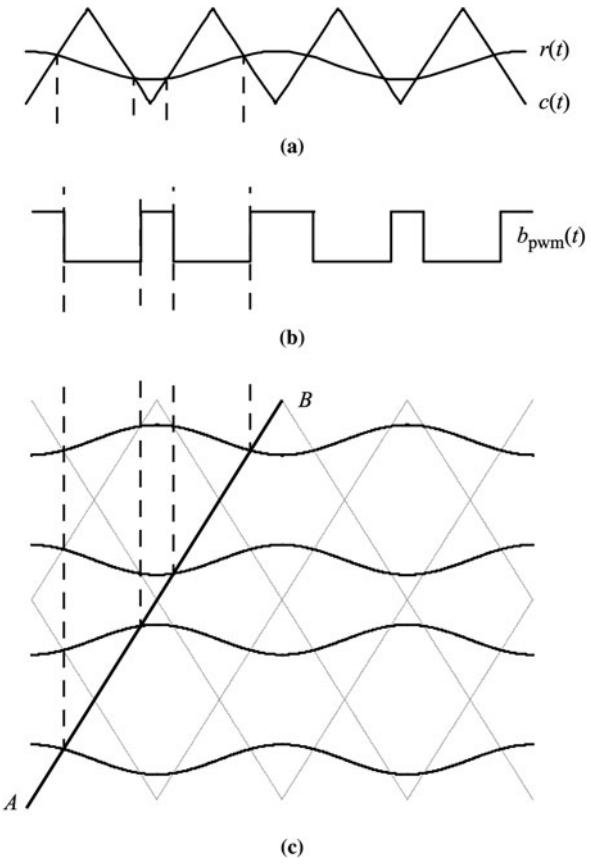

Fig. 2.4 CF double-edge modulation and its alternative representation for the development of a double Fourier series

defined above, and the intersection area, defined mathematically by

$$f(2\pi f_1 t + \theta_1, 2\pi f_c t + \theta_c), \tag{2.6}$$

has the same shape as the PWM waveform. Therefore, a spectral model is obtained for the PWM waveform when x and y in the double Fourier series representation of $f(x, y)$ are replaced by $x = 2\pi f_1 t + \theta_1$ and $y = 2\pi f_c t + \theta_c$, respectively. Note again that there is no need to explicitly define the PWM waveform and no limitations are imposed on the relationship between the carrier and the reference fundamental frequency.

With some minor modification of the two-dimensional function, the same procedure can be applied to other PWM methods. Although natural-sampling PWM has been assumed in the development so far, the method can be applied to regular-sampled PWM by using the sampled form instead of the original references.

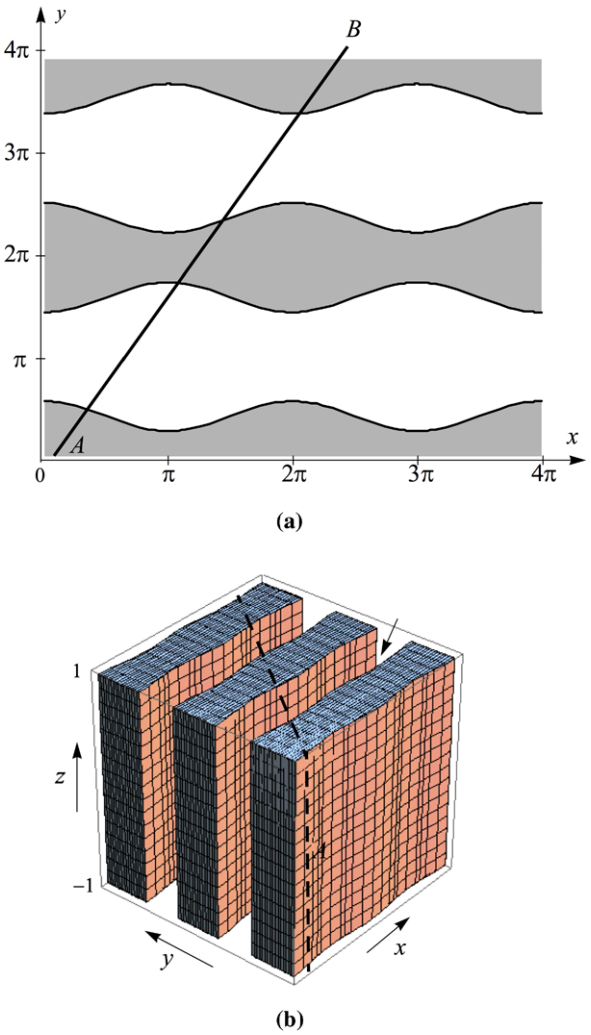

Fig. 2.5 Definition of a two-dimensional function $f_k(x, y)$ for double Fourier analysis

2.2.2 PWM Spectral Models

Double Fourier series models are given below for commonly used constant-frequency PWM methods. The reference is assumed to be defined by (2.2) in general. For the convenience of application in different power electronic circuits, we will consider

- *Unipolar modulation*: The carrier changes between 0 and a positive peak (C_m); the reference is always positive; and the PWM output switches between 0 and 1; and

- *Bipolar modulation*: The carrier is symmetric about zero, with a amplitude equal to C_m; the reference is a sine wave without DC offset; and the PWM output switches between $-1/2$ and $+1/2$.

The angular frequency of the carrier and the reference will be denoted $\omega_c (= 2\pi f_c)$ and $\omega_1 (= 2\pi f_1)$, respectively, and will be used in place of f_c and f_1 when it is convenient. The initial phase angles of the carrier and the reference (denoted by θ_1 and θ_c) will be assumed nonzero in general. Two additional parameters as defined below are also used to simplify the expressions:

- The average duty ratio:

$$D = \frac{R_0}{C_m}; \tag{2.7}$$

- The modulation index:

$$M = \frac{2R_1}{C_m}. \tag{2.8}$$

Each spectral model also involves Bessel functions of the first kind, $J_n(z)$, defined as follows:

$$J_n(z) = \frac{\mathrm{j}^{-n}}{\pi} \int_0^{2\pi} \mathrm{e}^{\mathrm{j}z\cos\theta} \mathrm{e}^{\mathrm{j}n\theta}\, \mathrm{d}\theta. \tag{2.9}$$

This function arises from the double integral involved in the definition of the double Fourier series coefficients (2.4) and (2.5). The argument z can be a real or complex number, and the function is real-valued if z is real. The other argument, n, is real and will always be an integer in the applications discussed here. Characteristics of the Bessel functions will be reviewed in the next subsection.

1. Unipolar Trailing-Edge Modulation, see Fig. 2.6:

$$\begin{aligned} b_{\mathrm{pwm}}(t) = D &+ \frac{M}{2}\cos(\omega_1 t + \theta_1) \\ &+ \sum_{m=1}^{+\infty} \frac{1}{m\pi} \Big\{ \sin\big[m(\omega_c t + \theta_c)\big] \\ &- J_0(m\pi M) \sin\big[m(\omega_c t + \theta_c) - 2mD\pi\big] \Big\} \\ &+ \sum_{m=1}^{+\infty} \sum_{n=\pm 1}^{\pm\infty} \frac{J_n(m\pi M)}{m\pi} \\ &\times \sin\left[\frac{n\pi}{2} - m(\omega_c t + \theta_c) - n(\omega_1 t + \theta_1) + 2mD\pi\right]. \end{aligned} \tag{2.10}$$

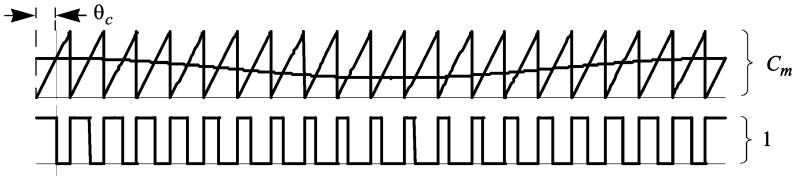

Fig. 2.6 Unipolar trailing-edge modulation using a sawtooth carrier

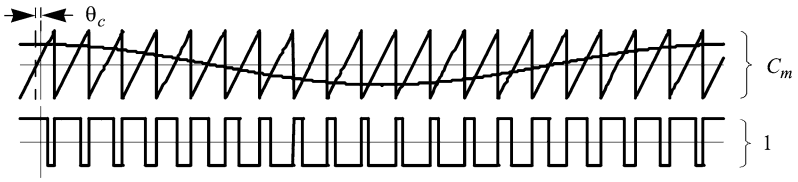

Fig. 2.7 Bipolar trailing-edge modulation using a sawtooth carrier

2. Bipolar Trailing-Edge Modulation, see Fig. 2.7 with $R_0 = 0$:

$$\begin{aligned} b_{\text{pwm}}(t) = {} & \frac{M}{2}\cos(\omega_1 t + \theta_1) \\ & + \sum_{m=1}^{+\infty} \frac{1}{m\pi}\big[\cos(m\pi) - J_0(m\pi M)\big]\sin\big[m(\omega_c t + \theta_c)\big] \\ & + \sum_{m=1}^{+\infty}\sum_{n=\pm 1}^{\pm\infty} \frac{J_n(m\pi M)}{m\pi}\sin\left[\frac{n\pi}{2} - m(\omega_c t + \theta_c) - n(\omega_1 t + \theta_1)\right]. \end{aligned} \tag{2.11}$$

3. Unipolar Leading-Edge Modulation, see Fig. 2.8:

$$\begin{aligned} b_{\text{pwm}}(t) = {} & D + \frac{M}{2}\cos(\omega_1 t + \theta_1) \\ & - \sum_{m=1}^{+\infty} \frac{1}{m\pi}\big\{\sin\big[m(\omega_c t + \theta_c)\big] \\ & - J_0(m\pi M)\sin\big[m(\omega_c t + \theta_c) + 2mD\pi\big]\big\} \\ & - \sum_{m=1}^{+\infty}\sum_{n=\pm 1}^{\pm\infty} \frac{J_n(m\pi M)}{m\pi} \\ & \times \sin\left[\frac{n\pi}{2} - m(\omega_c t + \theta_c) - n(\omega_1 t + \theta_1 + \pi) - 2mD\pi\right]. \end{aligned} \tag{2.12}$$

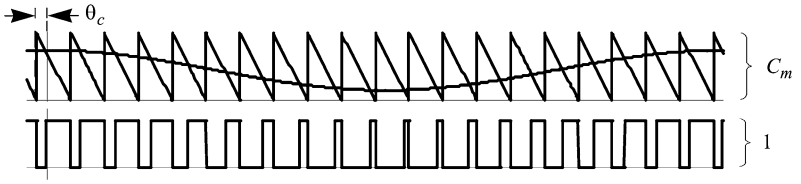

Fig. 2.8 Unipolar leading-edge modulation using a sawtooth carrier

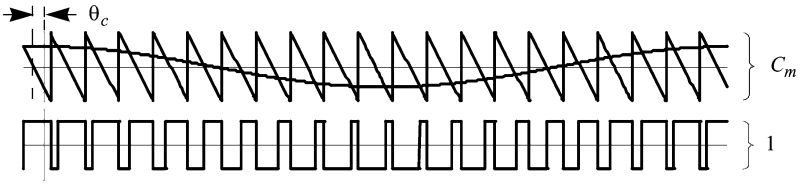

Fig. 2.9 Bipolar leading-edge modulation using a sawtooth carrier

4. Bipolar Leading-Edge Modulation, see Fig. 2.9 with $R_0 = 0$:

$$\begin{aligned} b_{\text{pwm}}(t) = {} & \frac{M}{2}\cos(\omega_1 t + \theta_1) \\ & - \sum_{m=1}^{+\infty} \frac{1}{m\pi}\big[\cos(m\pi) - J_0(m\pi M)\big]\sin\big[m(\omega_c t + \theta_c)\big] \\ & - \sum_{m=1}^{+\infty}\sum_{n=\pm 1}^{\pm\infty} \frac{J_n(m\pi M)}{m\pi} \\ & \times \sin\left[\frac{n\pi}{2} - m(\omega_c t + \theta_c) - n(\omega_1 t + \theta_1 + \pi)\right]. \end{aligned} \tag{2.13}$$

5. Unipolar Double-Edge Modulation, see Fig. 2.10:

$$\begin{aligned} b_{\text{pwm}}(t) = {} & D + \frac{M}{2}\cos(\omega_1 t + \theta_1) \\ & + \sum_{m=1}^{+\infty} \frac{2}{m\pi} J_0\left(\frac{m\pi M}{2}\right)\sin(Dm\pi)\,\cos\big[m(\omega_c t + \theta_c)\big] \\ & + \sum_{m=1}^{+\infty}\sum_{n=\pm 1}^{\pm\infty} \frac{2}{m\pi} J_n\left(\frac{m\pi M}{2}\right)\sin\frac{(2Dm+n)\pi}{2} \\ & \times \cos\big[m(\omega_c t + \theta_c) + n(\omega_1 t + \theta_1)\big]. \end{aligned} \tag{2.14}$$

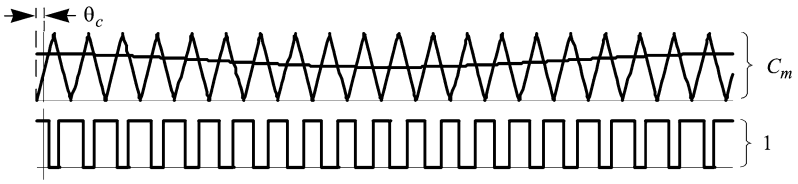

Fig. 2.10 Unipolar leading-edge modulation using a sawtooth carrier

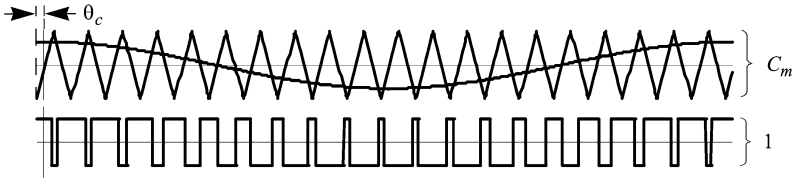

Fig. 2.11 Bipolar double-edge modulation using a triangle carrier

6. Bipolar Double-Edge Modulation, see Fig. 2.11 with $R_0 = 0$:

$$
\begin{aligned}
b_{\text{pwm}}(t) = {} & \frac{M}{2}\cos(\omega_1 t + \theta_1) \\
& + \sum_{m=1}^{+\infty} \frac{2}{m\pi} J_0\left(\frac{m\pi M}{2}\right) \sin\frac{m\pi}{2} \cos\big[m(\omega_c t + \theta_c)\big] \\
& + \sum_{m=1}^{+\infty} \sum_{n=\pm 1}^{\pm\infty} \frac{2}{m\pi} J_n\left(\frac{m\pi M}{2}\right) \sin\frac{(m+n)\pi}{2} \\
& \times \cos\big[m(\omega_c t + \theta_c) + n(\omega_1 t + \theta_1)\big]. \qquad (2.15)
\end{aligned}
$$

The double Fourier analysis method can also be used to develop spectral models for regular-sampled PWM by replacing the reference functions by their sampled version [9]. The method is also applicable when the reference contains more than one sine component (as long as it is periodic). However, the double integrals cannot be simplified by using the Bessel functions when the reference contains more than one sine component. Nevertheless, the double integral formulation in that case still provides a simple way to define the spectral model and can be evaluated numerically when quantitative analysis is needed.

2.2.3 Spectral Characteristics of PWM Converters

Each of the spectral models (2.10)–(2.13) contains a component that is in-phase with the sinusoidal component in the reference. The amplitude of this component,

$$\frac{M}{2} = \frac{R_1}{C_m},$$

is equal to that of the reference scaled down by the amplitude of the carrier. A DC component also exists in the PWM output under unipolar modulation, and its ratio to the DC component in the reference is equal to the reciprocal of the amplitude of the carrier, the same as that for the sine component. This linear relationship is an important characteristic of constant-frequency PWM and will be further discussed in the next section on small-signal modelling.

Besides the DC and the fundamental sine component, each PWM waveform contains many harmonics which can be grouped as follows:

1. Carrier frequency and its harmonics, at frequencies $f = mf_c, m = 1, 2, \ldots, +\infty$. These components exist regardless whether the reference is constant or variable.
2. Sideband harmonics of the carrier and its harmonics, at frequencies $f = mf_c + nf_1, n = \pm 1, \pm 2, \ldots, \pm\infty$.

The sideband harmonics only appear when the reference is modulated. The amplitude of the sideband harmonic at frequency $f = mf_c + nf_1$ is equal to

$$\frac{J_n(m\pi M)}{m\pi} \tag{2.16}$$

for leading- or trailing-edge modulation, and to

$$\frac{2}{m\pi} J_n\left(\frac{m\pi M}{2}\right) \tag{2.17}$$

for double-edge modulation. Note that (2.17) can be converted to (2.16) by redefining the parameter M for double-edge modulation. Additionally, since

$$\left|J_n(x)\right| = \left|J_{-n}(x)\right| \tag{2.18}$$

the sideband harmonic at frequency $f = mf_c + nf_1$ has the same magnitude as that at frequency $f = mf_c - nf_1$ for any integer m and n; in other words, sideband harmonics appear in pairs and are symmetric about each carrier harmonic. Figure 2.12 depicts Bessel functions $J_0(x)$ through $J_{10}(x)$ to show their basic characteristics.

Unipolar modulation is usually used in DC–DC converters where the reference is constant except during transient. The sideband harmonics in this case are instrumental in explaining the time-varying behaviour in small-signal analysis when the perturbation frequency approaches half the switching frequency, which will be discussed in the next section. Bipolar modulation, on the other hand, is commonly used in PWM inverters and rectifiers. A basic building block for such converters is the

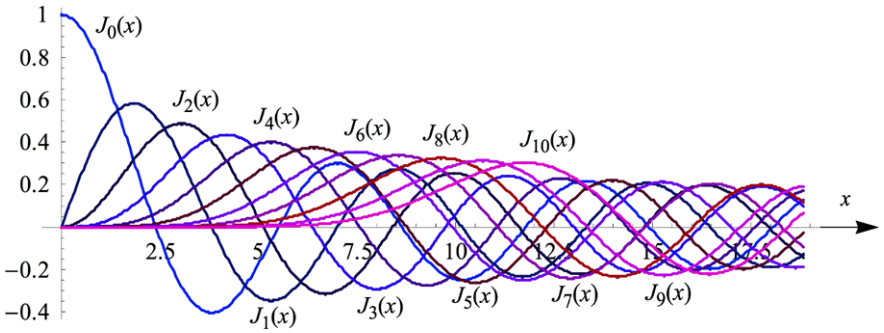

Fig. 2.12 A plot of Bessel functions $J_0(x)$ through $J_{10}(x)$

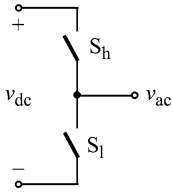

Fig. 2.13 A half-bridge circuit serving as a basic building block for AC–DC interface

half-bridge circuit depicted in Fig. 2.13. The AC terminal is alternately connected to the positive and the negative terminal of the DC link depending on whether the upper-side switch, S_h, or the lower-side switch, S_l, is turned on. Usually the two switches are controlled by complementary gate signals such that at any time one and only one switch conducts. If the middle of the DC link is used as the reference point and a bipolar PWM signal $v_{\text{pwm}}(t)$ defined in the previous subsection is applied to the upper switch, the DC and the AC voltages are related to each other by

$$v_{\text{ac}}(t) = v_{\text{dc}}(t)v_{\text{pwm}}(t). \tag{2.19}$$

With a constant DC-link voltage, v_{ac} is proportional to the PWM signal such that a spectral model can be readily obtained for v_{ac} from the bipolar PWM spectral models developed in the previous subsection. Therefore, the performance of the three bipolar PWM methods can be compared on the basis of their spectral models (2.11), (2.13) and (2.15). To that end, note first that the carrier harmonics and their sideband harmonics produced by trailing-edge bipolar PWM are equal in amplitude to the corresponding harmonics in leading-edge modulation. Hence these two methods have the same performance as far as harmonics are concerned. To compare them with double-edge bipolar modulation, the amplitudes of the first three carrier harmonics ($m = 1, 2, 3$) and their sideband components are tabulated in Table 2.1 for $n = \pm 1, \pm 2, \pm 3$. The comparison shows that double-edge modulation produces far fewer harmonics. In particular, the harmonic at frequency $f = mf_c + nf_1$ is zero if $m + n$ is even because the amplitude of the harmonic

Table 2.1 Comparison of carrier and sideband harmonics predicted by (2.11) and (2.15)

n	$m=1$, (2.11)	$m=1$, (2.15)	$m=2$, (2.11)	$m=2$, (2.15)	$m=3$, (2.11)	$m=3$, (2.15)
−3	0.0697	0	0.0573	0.0697	0.0279	0
−2	0.1426	0.1099	0.0059	0	0.0236	0.0881
−1	0.1572	0	0.0526	0.1572	0.0154	0
0	0.3008	0.4090	0.1860	0	0.1338	0.0853
1	0.1572	0	0.0526	0.1572	0.0154	0
2	0.1426	0.1099	0.0059	0	0.0236	0.0881
3	0.0697	0	0.0573	0.0697	0.0279	0

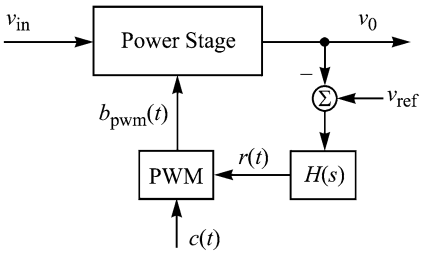

Fig. 2.14 A pulse-width modulator as part of a feedback control system

includes the term

$$\sin\frac{(m+n)\pi}{2} \tag{2.20}$$

which is zero when $m+n$ is even. In other words, double-edge modulation eliminates all even-order sideband harmonics of even-order carrier harmonics, as well as odd-order sideband harmonics of odd-order carrier harmonics. The reduced harmonic content is a significant advantage of double-edge modulation and makes the method more attractive for AC–DC and DC–AC converter application.

2.3 Small-Signal Modelling

Pulse-width modulator is an integral part of feedback control in power electronics. The reference signal, $r(t)$, used in the spectral analysis in the previous section is usually the output of a feedback controller (compensator), as depicted in Fig. 2.14 where $H(s)$ denotes the feedback controller transfer function. The modulation process itself, as demonstrated by the spectral models presented in the previous section, is highly nonlinear. Since most practical designs use linear control, a linear, time-invariant model that captures the small-signal behaviour of a modulator is needed for converter-level analysis and control design. Such small-signal models are developed in this section for both constant-frequency and variable-frequency PWM. The second topic treated here is interleaving—the operation of multiple pulse-width

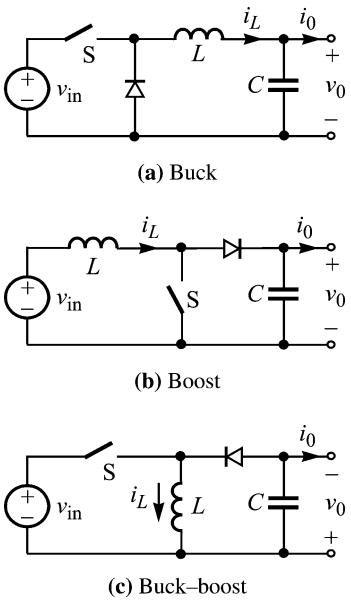

Fig. 2.15 Basic DC–DC converter topologies

modulators with phase-shifted carrier signals. We will briefly discuss the application of interleaving in parallel- and series-connected converters, and use the spectral models developed in the previous section to characterise the harmonica cancellation effects resulting from different interleaving arrangements.

2.3.1 Small-Signal Modelling of Constant-Frequency PWM

A PWM-controlled converter can be described by a set of linear differential equations in each conduction state of the switches if all components are linear and the switches (including diodes) are assumed ideal. The number of possible conduction states depends on the number of switches and the operation pattern of the converter. Figure 2.15 depicts three basic DC–DC converter circuits each of which uses one switch and one diode. In the continuous conduction mode (CCM) of operation [23], that is, when the inductor current flows continuously, the diode conducts whenever the switch is OFF, such that there are only two possible conduction states over a switching cycle: (a) the switch is ON and the diode is OFF; (b) the switch is OFF and the diode is ON. With the inductor current (i_L) and the output capacitor voltage (v_0) modelled as state variables, each of these converters can be described by two state-space models as follows where $x = (i_L, v_0)^\top$, $u = (v_{\text{in}}, i_0)^\top$:

$$\dot{x} = A_0 x + B_0 u \tag{2.21}$$

when the switch is OFF, and

$$\dot{x} = A_1 x + B_1 u \tag{2.22}$$

when the switch is ON. Denoting the unipolar PWM signal that drives the switch as $s(t)$, that is, $s(t) = 0$ when the switch is OFF and $s(t) = 1$ when the switch is ON, one can combine the two equations as follows:

$$\dot{x} = \big[A_0 + (A_1 - A_0)s(t)\big]x + \big[B_0 + (B_1 - B_0)s(t)\big]u. \tag{2.23}$$

This model is not amenable to linear control design due to the time-varying control function $s(t)$ being multiplied with the state and input variables. A standard technique to deal with such time-varying problem is averaging [6]. In this method, the right-hand side of (2.23) is replaced by its "moving" average over a switching cycle, resulting in the so-called state-space averaged model where the binary switching function $s(t)$ is replaced by its algebraic average over a switching cycle, that is, the duty ratio d of the switch [6]:

$$\frac{\mathrm{d}}{\mathrm{d}t}\langle x\rangle = \big[A_0 + (A_1 - A_0)d\big]\langle x\rangle + \big[B_0 + (B_1 - B_0)d\big]u. \tag{2.24}$$

The duty ratio is the control variable in the new averaged model, which is nonlinear in general due to the presence of the product between the duty ratio and the state variables.[1] A linear model suitable for linear control design can be obtained by conventional small-signal linearisation about a given operation point. Since it is the modulator reference, $r(t)$, that is actually controlled, a transfer function from the modulator input to the duty ratio of its PWM output is needed to complete such a small-signal model. This transfer function is usually referred to as the *modulator gain* and can be developed in either the time or the frequency domain.

To develop the modulator gain in the time domain, assume the reference consists of a constant, R_0, corresponding to the DC operation point of the converter about which the small-signal model is being developed. The corresponding steady-state duty ratio is denoted as D. Consider now that a small-signal perturbation, $\hat{R}$, is added to the reference. It's a matter of simple algebra to show that the corresponding perturbation in the duty ratio is

$$\hat{d} = \frac{\hat{R}}{C_m} \tag{2.25}$$

for any of the constant-frequency PWM methods reviewed in Sect. 2.1. Therefore, the gain of a CF pulse-width modulator is the reciprocal of the amplitude, C_m, of the carrier signal regardless what form of carrier is used.

To develop a small-signal modulator model in the frequency domain, consider a reference defined by (2.2) where the DC component, R_0, corresponds to the steady-state operation point and the second term defines a small-signal perturbation at frequency f_1. Each of the spectral models (2.10)–(2.15) developed in the previous

[1] An exception is the buck converter and its derivatives where switching only changes the connection of the input voltage to the converter. Therefore, the only nonlinear term in the averaged model is the product between the duty ratio and the input voltage, and the model is linear if the input voltage is assumed constant.

section contains a component at the same frequency and is in-phase with the perturbation in $r(t)$. The amplitude of this perturbation term is equal to

$$\frac{M}{2} = \frac{R_1}{C_m} \tag{2.26}$$

which shows again that the modulator gain is $1/C_m$ regardless the form of the carrier signal.

The discussion above did not consider possible sideband components that could appear at the perturbation frequency and affect the small-signal response of the modulator. Based on (2.10)–(2.15), the frequency of the sideband components can be written as

$$mf_c + nf_1, \quad m = 1, 2, \ldots, +\infty, \; n = \pm 1, \pm 2, \ldots, \pm\infty. \tag{2.27}$$

When the perturbation frequency, f_1, is at half the carrier frequency, for example, the frequency of the sideband component corresponding to $m = 1$ and $n = -1$ is

$$f = f_c - f_1 = 2f_1 - f_1 = f_1, \tag{2.28}$$

which is the same as the perturbation frequency. For unipolar trailing-edge modulation, this sideband component is

$$-\frac{J_{-1}(\pi M)}{\pi} \cos[\omega_1 t - \theta_1 + \theta_c - 2D\pi].$$

The coincidence of such a sideband component with the response of the modulator at the perturbation frequency presents several problems for linear analysis:

1. The amplitude of the sideband component is a nonlinear function of the perturbation;
2. The phase difference to the reference, $2\theta_1 - \theta_c + 2D\pi$, is not constant and depends on the initial phase of the perturbation as well as the carrier.

The nonlinear amplitude can be replaced by a linear approximation of the Bessel function under small-signal assumption, that is, by assuming $M \ll 1$. However, the variable phase angle indicates that the response of the modulator at the perturbation frequency is dependent of the initial phase angle of the perturbation. Such time-varying behaviour violates the underlying assumption for linear analysis and represents a fundamental limitation of the small-signal linear model and the associated linear control design techniques for PWM converters.

In general, a sideband component at frequency $mf_c + nf_1$ will appear at the perturbation frequency, f_c, if the latter is such that

$$f_1 = \frac{mf_c}{1-n}, \quad m = 1, 2, \ldots, +\infty, \; n = 0, -1, -2, \ldots, -\infty. \tag{2.29}$$

However, since the amplitude of the sideband component at frequency is proportional to Bessel function $J_n(x)$ and the lowest-order term in the Taylor expansion of

$J_n(x)$ is proportional to

$$\frac{x^{|n|}}{2^{|n|}n!}, \tag{2.30}$$

the contribution of such a sideband component to the modulator response at the perturbation frequency can be ignored for the purpose of small-signal analysis except for the cases of $n = 0$ and $n = -1$, in other words, when the perturbation frequency is a multiple of half the carrier frequency:

$$f_1 = \frac{mf_c}{2}, \quad m = 1, 2, \ldots, +\infty. \tag{2.31}$$

The above equation indicates that the lowest frequency at which small-signal response of a pulse-width modulator is affected by sideband components and is no longer time-invariant is half the carrier frequency. This places an upper frequency limit on the validity of averaged models of PWM converters. Nonlinear control methods that overcome this limit of linear models are discussed in other chapters of this book.

Averaging effectively removes the switching ripple in the responses of a converter. If necessary, the ripple can be recovered from the averaged model. A method [16] to reconstruct switching ripple from the averaged model of a PWM converter will be discussed in Sect. 2.4 in conjunction with modelling of peak-current control.

The straightforward state-space averaging method as used above is only applicable to PWM converters operating in the continuous conduction mode. In the discontinuous conduction mode (DCM), the inductor current returns to zero in each switching cycle such that the diode only conducts for a portion of the interval in which the switch is OFF. This leads to a third interval over a switching cycle in which both the switch and the diode are OFF. The state-space model of the converter in this third interval needs to be included in the averaged model. Additionally, since the length of the conduction interval of the diode depends on several parameters and is not constant, a so-called duty ratio constraint is needed to relate the duty ratio of the diode to other variables in order to completely define the averaged model. These are discussed in reference [23], which also includes analytical small-signal models for the three basic converters shown in Fig. 2.15.

A major focus of power electronics research in the 1980s and 1990s was the development of various resonant-type converters. The basic idea of resonant converters is to create a resonance in the voltage or current of a switch by using additional passive and/or active devices. The resonant response causes the switch voltage or current to naturally return to zero, thereby allowing the switching operation to occur under zero-voltage or zero-current conditions to significantly reduce the switching transition loss. Averaged modelling of resonant converters is complicated by the presence of additional time constants of the resonant circuit. Singular perturbation theory and time-scale separation techniques can be applied to deal with such multiple-time-scale systems and to develop averaged models that can be used for linear control design [21]. The modulator model presented above can still be

used. Some resonant converters, such as quasi-resonant and load-resonant converters, require variable-frequency PWM control, which will be discussed in the next subsection.

The control method depicted in Fig. 2.14 is essentially the voltage-mode control, in which the switch duty ratio is derived directly from the error signal of the output voltage. The duty ratio to output voltage transfer function, which can be obtained from the small-signal linearised averaged model, is of second-order for second-order converters such as those depicted in Fig. 2.15, with highly under-damped resonant poles. It is difficult to achieve fast control for such second-order systems because the crossover frequency of the voltage control loop usually has to be kept below the power stage resonant frequency in order to ensure sufficient stability margin. An additional difficulty of voltage-mode control for boost and buck–boost converters is the existence of a right half-plane (RHP) zero in the duty ratio to output voltage transfer function, which is usually at a frequency even lower than the power stage resonant frequency. Current-mode control, in which an additional loop is closed for the inductor current, can be used to solve these problems. Section 2.4 will present one of such current control methods, the peak-current control.

2.3.2 Small-Signal Modelling of Variable-Frequency PWM

The modulator gain developed in the previous subsection is valid for constant-frequency PWM. Variable-frequency modulators exhibit unique features in their small-signal behaviour and are modelled here.

Consider first the constant-OFF-time VF PWM, which is illustrated in Fig. 2.16 for two cases:

1. The reference $r(t)$ is constant;
2. The reference $r(t)$ consists of a constant and a small-signal perturbation, as defined by (2.2).

The resulting PWM outputs are shown as v_1 and v_2, respectively. By definition, the small-signal gain of the modulator is the ratio of the component in v_2 that is at the perturbation frequency, f_1, to the amplitude of the perturbation, R_1. For the purpose of small-signal modelling, it is assumed that the perturbation is much smaller than the constant, that is, $R_1 \ll R_0$. Additionally, the following variables are defined:

- The up-slope of the ramp signal, $c(t)$, is constant and is denoted as m_0.
- The steady-state ON-time (when $R_1 = 0$) is denoted as T_{ON}. It can be determined from Fig. 2.16 that

$$T_{\mathrm{ON}} = \frac{R_0}{m_0}.$$

- The constant OFF-time is equal to T_{OFF}. Denote $1/(T_{\mathrm{ON}} + T_{\mathrm{OFF}})$ by f_c, which is the steady-state carrier frequency of the modulator when the perturbation is not present ($R_1 = 0$).

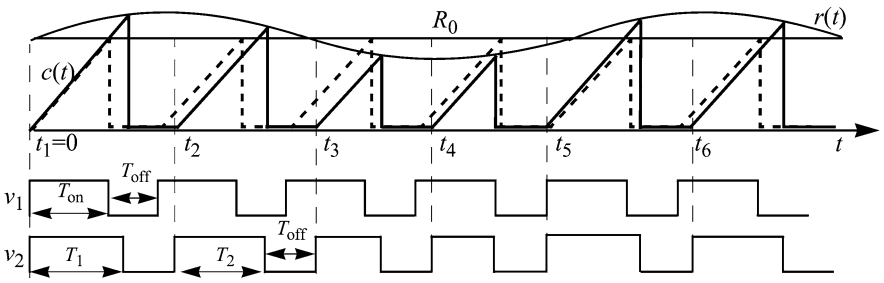

Fig. 2.16 Constant-OFF-time modulation. v_1: PWM output when the reference is a constant; v_2: PWM output when the reference $r(t)$ contains a sinusoidal perturbation

Using these notations, reference [14] developed the small-signal gain of the VF constant-OFF-time modulator as follows

$$\frac{1}{m_0(T_{\mathrm{ON}}+T_{\mathrm{OFF}})}\sin\frac{sT_{\mathrm{OFF}}}{\mathrm{j}2}\left(\sin\frac{s(T_{\mathrm{ON}}+T_{\mathrm{OFF}})}{\mathrm{j}2}\right)^{-1}\mathrm{e}^{\frac{sT_{\mathrm{ON}}}{2}}, \tag{2.32}$$

where $\mathrm{j}=\sqrt{-1}$ is the imaginary unit. Compared to the constant-frequency modulator gain developed in the previous subsection, this gain is much more complicated and exhibits nonlinear characteristics that are frequency dependent.

Defining a function $K_1(s)$ as

$$K_1(s)=\frac{T_{\mathrm{ON}}+T_{\mathrm{OFF}}}{T_{\mathrm{OFF}}}\sin\frac{sT_{\mathrm{OFF}}}{\mathrm{j}2}\left(\sin\frac{s(T_{\mathrm{ON}}+T_{\mathrm{OFF}})}{\mathrm{j}2}\right)^{-1}, \tag{2.33}$$

the modulator gain (2.33) can be written as

$$\Gamma_1(s)=\frac{T_{\mathrm{OFF}}}{m_0(T_{\mathrm{ON}}+T_{\mathrm{OFF}})^2}K_1(s)\mathrm{e}^{\frac{sT_{\mathrm{ON}}}{2}}. \tag{2.34}$$

Note that $\Gamma_1(s)$ consists of three parts:

1. $T_{\mathrm{OFF}}/[m_0(T_{\mathrm{ON}}+T_{\mathrm{OFF}})^2]$, which is independent of the frequency and represents the DC gain of the modulator. The DC gain can also be derived by taking the derivative of the steady-state duty ratio with respect to the modulator input, R_0 (note that $T_{\mathrm{ON}}=R_0/m_0$):

$$\frac{\mathrm{d}}{\mathrm{d}R_0}\left(\frac{T_{\mathrm{ON}}}{T_{\mathrm{ON}}+T_{\mathrm{OFF}}}\right)=\frac{\mathrm{d}}{\mathrm{d}R_0}\left(\frac{R_0/m_0}{R_0/m_0+T_{\mathrm{OFF}}}\right)=\frac{T_{\mathrm{OFF}}}{m_0(T_{\mathrm{ON}}+T_{\mathrm{OFF}})^2}.$$

   This can be compared with the gain of constant-frequency pulse-width modulators, which, using the notations introduced here, can be written as $[m_0(T_{\mathrm{ON}}+T_{\mathrm{OFF}})]^{-1}$.
2. The second part, represented by $K_1(s)$, is frequency-dependent but is always real-valued, hence does not contribute to the phase response of the modulator gain. Its magnitude is close to unity except at frequencies approaching half the switching frequency.

3. The third part in (2.34) does not contribute to the amplitude of the gain. It corresponds to a phase lead that increases linearly with the frequency as well as the ON-time, T_{ON}.

The phase lead is the most interesting part of the VF PWM gain and represents an advantage of the modulation method because it helps to increase the phase margin of the control loop. The phase lead is most significant at high frequencies and/or when T_{ON} is large. For example, at one tenth of the switching frequency, the phase lead will be 14.4° for $T_{\mathrm{ON}}/(T_{\mathrm{ON}} + T_{\mathrm{OFF}}) = 0.8$. This may have significant impact on loop design, especially when wide bandwidth is required.

The modulator gain for constant ON-time control can be obtained by exploiting the duality between constant ON-time and constant OFF-time control. To this end, assume that the same signal $r(t)$ as shown in Fig. 2.16 is now used to modulate the OFF-time while the ON-time is fixed at T_{ON}. Denoting the resulting constant ON-time PWM waveform as $\overline{p}(t, T_{\mathrm{ON}})$ and the original constant OFF-time PWM waveform as $p(t, T_{\mathrm{OFF}})$, one can see that $\bar{p}(t, T_{\mathrm{ON}}) = 1 - p(t, T_{\mathrm{OFF}})$ if T_{ON} under constant ON-time PWM is equal to T_{OFF} under constant OFF-time PWM. Therefore, the small-signal gain of a constant ON-time VF modulator can be obtained by exchanging T_{ON} and T_{OFF} in (2.32) and multiplying the resulting expression by -1, as given below:

$$\frac{-1}{m_0(T_{\mathrm{ON}} + T_{\mathrm{OFF}})} \sin \frac{sT_{\mathrm{ON}}}{\mathrm{j}2} \left(\sin \frac{s(T_{\mathrm{ON}} + T_{\mathrm{OFF}})}{\mathrm{j}2} \right)^{-1} \mathrm{e}^{\frac{sT_{\mathrm{OFF}}}{2}}. \tag{2.35}$$

Like in the case of constant OFF-time PWM, we can define a function

$$K_2(s) = \frac{T_{\mathrm{ON}} + T_{\mathrm{OFF}}}{T_{\mathrm{ON}}} \sin \frac{sT_{\mathrm{ON}}}{\mathrm{j}2} \left(\sin \frac{s(T_{\mathrm{ON}} + T_{\mathrm{OFF}})}{\mathrm{j}2} \right)^{-1}, \tag{2.36}$$

and rewrite (2.35) as follows:

$$\Gamma_2(s) = \frac{-T_{\mathrm{ON}}}{m_s(T_{\mathrm{ON}} + T_{\mathrm{OFF}})^2} K_2(s) \mathrm{e}^{\frac{sT_{\mathrm{OFF}}}{2}}. \tag{2.37}$$

Similar to $K_1(s)$, $K_2(s)$ is approximately equal to unity except at high frequencies. The phase of consists of two parts: a 180° phase reversal (due to the minus sign in front of the expression) and a phase lead that is proportional to the OFF-time. Hence it can be concluded that both constant OFF-time and constant ON-time VF PWM creates a phase lead which is beneficial for control stability.

Note that the term

$$\sin \frac{s(T_{\mathrm{ON}} + T_{\mathrm{OFF}})}{\mathrm{j}2} \tag{2.38}$$

appears as a denominator in both $K_1(s)$ and $K_2(s)$. This term becomes zero at frequencies

$$s = \frac{\mathrm{j}2k\pi}{T_{\mathrm{ON}} + T_{\mathrm{OFF}}}, \tag{2.39}$$

that is, at multiples of the steady-state PWM frequency $f_c = 1/(T_{\mathrm{ON}} + T_{\mathrm{OFF}})$. This is, however, not a practical problem since the use of the small-signal model, as discussed in the previous section, should be limited to half the PWM frequency.

2.3.3 Interleaved PWM

When multiple PWM converters are connected in series or in parallel, it is advantageous to operate all converters at the same frequency but with certain phase shift among their PWM signals. The technique is referred to as interleaving and has been widely used in power electronics. The benefit of interleaving can be understood by an example shown in Fig. 2.17, where two identical buck converters operate in parallel with the same input and output voltage. Both converters operate with the same carrier frequency and reference (hence also duty ratio), but the two carrier signals are shifted from each other by half a carrier cycle. The resulting ripples (without the DC component) of the two inductor currents are shown at the bottom of Fig. 2.17. The output voltage is treated as a constant, and the two inductors are assumed identical. As can be seen, the combined current, i_L, that charges the output capacitor has much smaller ripple, and the ripple is cancelled completely when the duty ratio is 0.5.

Similar effects can be observed in the input current, i_{in}, of the two parallel buck converters. The same technique can be applied to other DC–DC converters. In general, with N identical converters operating in the parallel and their carrier signals being phase-shifted from each other by one Nth of a carrier cycle, the fundamental frequency of the combined input or output current is Nf_c, where f_c is the carrier frequency individual converters are switched at. This ripple cancellation effect can be exploited to reduce input and output filtering requirements.

The effects of interleaving on current ripple can also be analysed in the frequency domain by using the PWM spectral models developed in the previous section.

Consider again the parallel buck converters shown in Fig. 2.17. Response of each of the inductor currents can be written as

$$L_1 \frac{\mathrm{d}}{\mathrm{d}t} i_{L1} = v_{\mathrm{in}} s_1(t) - v_0,$$

$$L_2 \frac{\mathrm{d}}{\mathrm{d}t} i_{L2} = v_{\mathrm{in}} s_2(t) - v_0,$$

where $s_1(t)$ and $s_2(t)$ are the switching functions of switch S_1 and S_2 as defined in Fig. 2.17. Assuming $L_1 = L_2 = L$, we obtain the response of the combined current i_L as follows:

$$L \frac{\mathrm{d}}{\mathrm{d}t} i_L = v_{\mathrm{in}} \big[s_1(t) + s_2(t) \big] - 2v_0. \tag{2.40}$$

With constant input and output voltages, (2.40) indicates that the cancellation of harmonics in current i_L is due to the cancellation of harmonics in the PWM functions

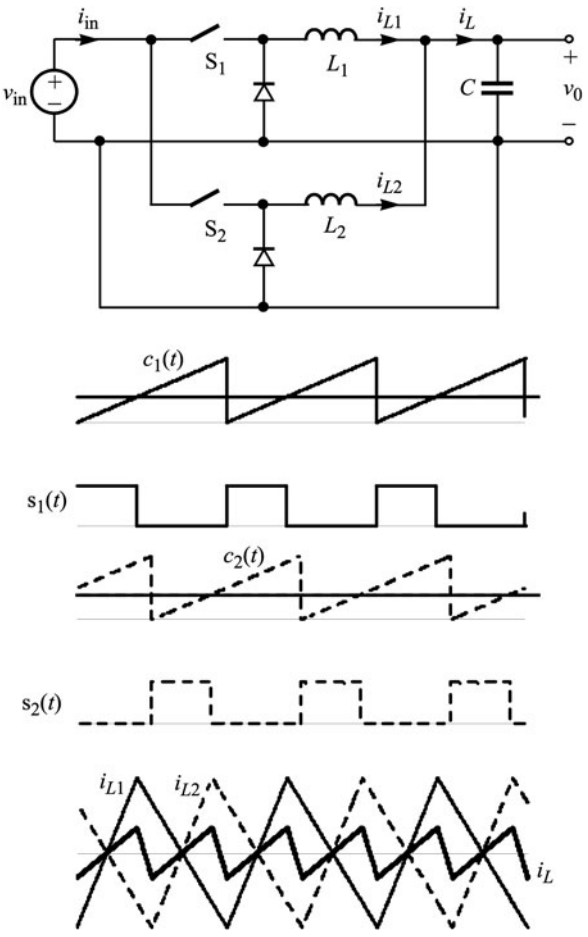

Fig. 2.17 Two buck converters operate in parallel and the resulting ripple cancellation effect through interleaving

$s_1(t)$ and $s_2(t)$. Consider the unipolar trailing-edge PWM spectral model (2.10), which simplifies to

$$b_{\text{pwm}}(t) = D + \sum_{m=1}^{+\infty} \frac{2\sin(mD\pi)}{m\pi} \cos\big[m(\omega_c t + \theta_c) - mD\pi\big]$$

when the reference is constant ($M = 0$). Without losing generality, assume the initial phase angle of the first carrier signal, $c_1(t)$, is zero, that is, $\theta_{c1} = 0$. The second carrier signal, $c_2(t)$, is delayed from $c_1(t)$ by half a carrier cycle, hence $\theta_{c2} = -\pi$. Therefore,

$$s_1(t) = D + \sum_{m=1}^{+\infty} \frac{2\sin(mD\pi)}{m\pi} \cos[m\omega_c t - mD\pi], \tag{2.41}$$

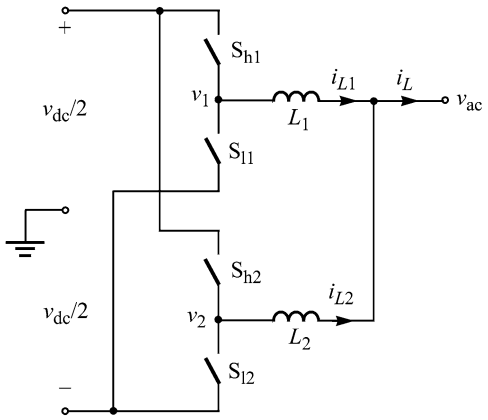

Fig. 2.18 Two half-bridge converters connected in parallel through inductors on the AC side

$$s_2(t) = D + \sum_{m=1}^{+\infty} \frac{2\sin(mD\pi)}{m\pi} \cos\left[m\omega_c t - m(D+1)\pi\right], \tag{2.42}$$

which indicates that all odd-order harmonics of the carrier are eliminated in $s_1(t) + s_2(t)$; in other words, the lowest-order harmonic in the combined output current is at twice the carrier frequency.

The frequency-domain analysis presented above can be generalised to any number of parallel converters as well as to other converter topologies. It is especially effective for interleaved AC–DC and DC–AC converters where the varying ripple pattern makes it difficult to study the ripple cancellation effects in the time domain.

As an example, consider the case when two of the half-bridge converter shown in Fig. 2.13 are connected in parallel, as depicted in Fig. 2.18. The DC input terminals are connected together directly. To prevent short circuit, an inductor has to be inserted at the output of each converter before the two can be connected in parallel. Assume each pair of switches are controlled by a bipolar double-edge modulator. Further, assume the reference for both modulators is $r(t) = R_1 \cos(2\pi f_1 t + \theta_1)$, and the triangle carriers have the same frequency and amplitude, but are phase shifted from each other by half a carrier cycle. Without losing generality, assume the initial phase angle of both the reference and the first carrier is zero. Based on the analyses presented in Sect. 2.2, the voltage produced by each half bridge relative to the middle of the DC link is

$$v_1(t) = \frac{v_{dc}}{2}\left[\frac{M}{2}\cos(\omega_1 t) + \sum_{m=1}^{+\infty} \frac{2}{m\pi} J_0\left(\frac{m\pi M}{2}\right) \sin\frac{m\pi}{2} \cos(m\omega_c t) \right.$$
$$\left. + \sum_{m=1}^{+\infty} \sum_{n=\pm 1}^{\pm\infty} \frac{2}{m\pi} J_n\left(\frac{m\pi M}{2}\right) \sin\frac{(m+n)\pi}{2} \cos(m\omega_c t + n\omega_1 t)\right], \tag{2.43}$$

$$v_2(t) = \frac{v_{\mathrm{dc}}}{2}\left[\frac{M}{2}\cos(\omega_1 t) + \sum_{m=1}^{+\infty}\frac{2}{m\pi}J_0\left(\frac{m\pi M}{2}\right)\sin\frac{m\pi}{2}\cos\big[m(\omega_c t-\pi)\big]\right.$$
$$+\sum_{m=1}^{+\infty}\sum_{n=\pm1}^{\pm\infty}\frac{2}{m\pi}J_n\left(\frac{m\pi M}{2}\right)\sin\frac{(m+n)\pi}{2}$$
$$\left.\times\cos\big[m(\omega_c t-\pi)+n\omega_1 t\big]\right]. \tag{2.44}$$

Similar to the case of two parallel buck DC–DC converters, harmonic cancellation between i_{L1} and i_{L2} can be studied based on harmonic cancellation between v_1 and v_2. By comparing the two expressions given above, it can be easily seen that interleaving cancels all odd-order harmonics of the carrier and all their sideband components. Further, since the amplitude of any even-order carrier harmonic is zero, the only harmonics remained in $v_1(t) + v_2(t)$ are the following odd-order sideband components of even-order carrier harmonics:

$$\frac{4v_{\mathrm{dc}}}{2}\sum_{m=2,4,\ldots}^{+\infty}\sum_{n=\pm1,\pm3,\ldots}^{\pm\infty}\frac{1}{m}J_n\left(\frac{m\pi M}{2}\right)\sin\frac{(m+n)\pi}{2}\cos(m\omega_c t+n\omega_1 t). \tag{2.45}$$

The above analysis can be extended to any number of parallel converters. The same analysis and ripple cancellation principle also apply to converters connected in series. In general, with N identical converters operating in either parallel or series, and their carrier shifted from each other by one Nth of a carrier cycle, all harmonics except those at N-multiples of the carrier frequency and their sideband components will be eliminated.

The interleaving method discussed so far confines the carrier phase shift to one Nth of a carrier cycle when N modules are connected. It has been recognised recently [15] that this may not be optimal. For example, the frequency range in which conducted electromagnetic interference (EMI) is measured by many EMI standards is from 150 kHz to 30 MHz. EMI filter size is typically driven by the lowest carrier harmonic within this frequency range. With three converters in parallel and each switching at 50 kHz, interleaving as discussed before would eliminate the first and the second carrier harmonics as well as their sideband components, but leaves the third carrier harmonic and its sideband components unaffected. Since the third carrier harmonic in this case (150 kHz) is right at the starting frequency of EMI measurement, interleaving doesn't help to reduce the EMI filter size.

For the above example, it would be more advantageous to reduce the third carrier harmonic and its sideband components. There are other applications where it is desirable to selectively reduce certain carrier harmonics and their sideband components. This can be achieved by the newly developed *asymmetric interleaving* method [1], in which the carrier phase shift is not confined to one Nth of a carrier cycle and can vary from one pair of converters to another. To distinguish from this new method, the interleaving method discussed before is called *symmetric inter-*

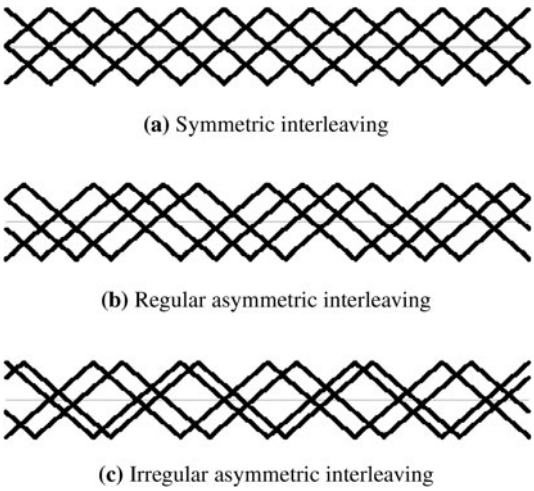

(a) Symmetric interleaving

(b) Regular asymmetric interleaving

(c) Irregular asymmetric interleaving

Fig. 2.19 Interleaving of four triangle carrier signals

leaving. Figure 2.19 illustrates the basic concept of asymmetric interleaving, which is further divided into two subcategories:

1. *Regular Asymmetric Interleaving*: Like symmetric interleaving, the phase shifts between adjacent converters are still equal in this case but they don't add to one carrier period. The carrier initial phase angle of the kth converter can be written as

$$\theta_{ck} = (k-1)\Delta\theta_c + \theta_{c1}, \quad k = 1, 2, \ldots, N, \tag{2.46}$$

   where $\Delta\theta_c$ is a constant,
2. *Irregular Asymmetric Interleaving*: The carrier phase shifts are not equal and don't necessarily add to one carrier period.

The harmonic cancellation effects of asymmetric interleaving among N parallel or series converters can be characterised by using the harmonic scaling factor defined below where is the initial phase angle of the kth converter [15]:

$$\kappa_m = \frac{1}{N}\sum_{k=1}^{N} \mathrm{e}^{\mathrm{j}m\theta_{ck}}. \tag{2.47}$$

The scaling factor allows the combined harmonic spectrum of N parallel or series converters to be determined from that of one converter by simply multiplying each harmonic by $N\kappa_m$. Note that κ_m applies to the mth carrier harmonic as well as all of its sideband components. Under symmetric interleaving, it can be verified that

$$\kappa_m = \begin{cases} 1 & \text{if } m = iN, \\ 0 & \text{if } m \neq iN, \end{cases} \tag{2.48}$$

Table 2.2 Harmonic scaling factors under regular asymmetric interleaving for the case of $N = 4$

m	$\Delta\theta_c$						
	18°	22.5°	30°	45°	75°	90°	110°
1	0.939	0.906	0.837	0.653	0.205	0	0.196
2	0.769	0.653	0.433	0.000	0.224	0	0.262
3	0.524	0.318	0.000	0.271	0.271	0	0.837
4	0.250	0.000	0.250	0.000	0.433	1	0.133
5	0.000	0.213	0.224	0.271	0.958	0	0.086
6	0.182	0.271	0.000	0.000	0.000	0	0.433
7	0.267	0.180	0.224	0.653	0.126	0	0.583
8	0.250	0.000	0.250	1.000	0.250	1	0.163
9	0.149	0.180	0.000	0.653	0.653	0	0.000
10	0.000	0.271	0.433	0.000	0.837	0	0.925

where i is any integer. In general, κ_m varies between 0 and 1, with 0 indicating complete cancellation of the mth carrier harmonic and all of its sideband components. Table 2.2 tabulates the value of κ_m under regular asymmetric interleaving with different values of $\Delta\theta_c$ for the case of $N = 4$.

2.4 Peak Current Control

The principle of peak-current control is illustrated in Fig. 2.20. Compared to the voltage-mode control depicted in Fig. 2.14, the inductor current is used here in place of the carrier signal to generate the PWM signal. The method works as follows: The switch is turned on by a clock signal at the beginning of each switching cycle. The sensed inductor current is compared to the output of the voltage compensator, denoted as i_p in Fig. 2.20, and the switch is turned off when the two become equal. For stability reasons, a compensation ramp with a slope equal to m_c is usually added to the sensed inductor current such that the inductor current is effectively compared to the reference minus the compensation ramp.

Peak-current control offers several practical advantages over voltage-mode control for DC–DC converters and other applications. Since the peak of the inductor current is directly controlled, it provides a built-in over-current protection for the switch and other components. The use of the inductor current in the pulse-width modulation process effectively introduces an inner feedback control loop that changes the control characteristics and simplifies the design of the output voltage feedback compensator. Additionally, the method is easy to implement since there is no need for an external ramp (carrier) signal for PWM. For these reasons, most power supplies used in practice are controlled by this method.

Peak-current control belongs to the general category of current-mode or current-programmed control [8]. Other current-mode control methods include average current control [7], nonlinear carrier control [11] and nonlinear average current con-

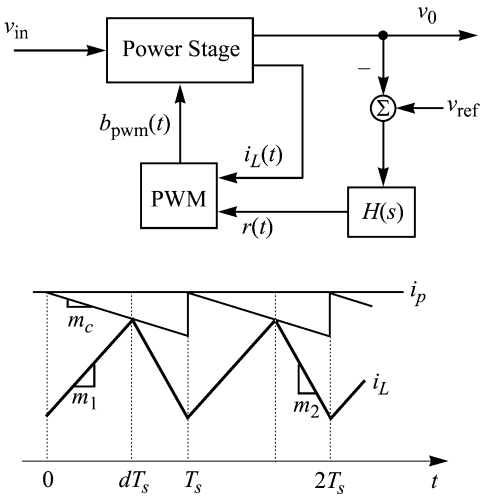

Fig. 2.20 Principle of peak-current control

trol [18]. These methods are particularly useful for rectifiers with active power factor correction (PFC). Modelling of peak-current control is included in this chapter because of its direct involvement in the pulse-width modulation process.

2.4.1 Averaged Modelling and Duty Ratio Constraint

The state-space averaged model developed in the previous section is still valid under peak-current control. However, to complete the model, a duty ratio constraint that relates the duty ratio, d, to other variables used in the averaged model is needed. Such a duty ratio constraint can be developed from the principle of the control method, and there are several different models in the literature. Early work on this subject developed the duty ratio constraint by assuming that the inductor current waveform is in a steady state [10]. With reference to Fig. 2.20,[2] the average of the inductor current, $\langle i_L \rangle$, can be related to other variables by the following equation if one assumes that the inductor current returns to its initial value at the end of each switching cycle, that is, when the current waveform has reached its steady state:

$$\langle i_L \rangle = i_p - \left(m_c + \frac{m_1}{2} \right) dT_s. \tag{2.49}$$

It was pointed out in [26] that using the steady-state current waveform is inconsistent with the objective of developing a dynamic model. Indeed, the resulting averaged model only predicts the DC and low-frequency behaviour of peak-current controlled DC–DC converters [17]. The duty ratio constraint proposed in [26] doesn't involve

[2]Note that all slopes defined in Fig. 2.20 (m_c, m_1 and m_2) are positive variables.

steady-state assumption and is given below:

$$\langle i_L \rangle = i_p - m_c d T_s + \frac{T_s}{2}\big[m_1 d^2 + m_2(1-d)^2\big]. \tag{2.50}$$

This results in improved accuracy of the averaged model in the high-frequency region. However, neither model can predict the subharmonic (ripple, switching) instability that is characteristic of peak-current control [8]. As a remedy for this limitation, an additional second-order transfer function representing the so-called sample-and-hold effects was proposed in [12] as part of the modulator gain, which complicates the model and has been a source of confusion.

The subharmonic instability problem can be explained with reference to the current waveform depicted in Fig. 2.20. Denote the value of the inductor current at the beginning of the kth switching cycle as $i_L[k]$. Without a compensation ramp, that is, when $m_c = 0$, the inductor current reaches the reference, i_p, when the switch turns off. Hence,

$$i_L[k] = d[k] m_1 T_s + i_p, \tag{2.51}$$

from which the duty ratio, $d[k]$, in the kth switching cycle can be found:

$$d[k] = \frac{i_p - i_L[k]}{m_1 T_s}. \tag{2.52}$$

To determine the value of the inductor current at the end of the kth switch cycle, denoted as $i_L[k+1]$, note that

$$i_L[k+1] = i_p - \big(1 - d[k]\big) m_2 T_s. \tag{2.53}$$

Substituting (2.52) into (2.53), we have

$$i_L[k+1] = -\frac{m_2}{m_1} i_L[k] + \left(1 + \frac{m_2}{m_1}\right) i_p - m_2 T_s. \tag{2.54}$$

This first-order sampled-data model indicates that the inductor current response is unstable if

$$-\frac{m_2}{m_1} \tag{2.55}$$

lies outside the unit circle, that is, if

$$\frac{m_2}{m_1} > 1. \tag{2.56}$$

To relate this instability condition to usual operation parameters of a converter, note that $m_1 d T_s = m_2(1-d)T_s$ holds when the inductor current is in steady-state such that

$$\frac{m_2}{m_1} = \frac{d}{1-d}, \tag{2.57}$$

which indicates that a peak-current controlled converter is inherently unstable when the duty ratio is larger than 50%.

2.4.2 Ripple Reconstruction from Averaged Models

Duty ratio constraints that enable an averaged model to predict subharmonic instability under peak-current control are introduced here. The method is based on reconstructing the ripple current of the inductor from the state-space averaged model and using the estimated ripple to define the duty ratio. The ripple estimation method is developed from a mathematical procedure called KBM (Krylov–Bogoliubov–Mitropolsky) algorithm [4]. The KBM algorithm is reviewed in the following while characteristics of the resulting averaged models will be presented in the next subsection.

Denote, for any of the second-order DC–DC converters shown in Fig. 2.15, the instantaneous inductor current as $i_L(t)$ and its local average as $\langle i_L(t)\rangle$. Under CCM operation, the converter can be described by the following piece-wise linear model

$$\frac{\mathrm{d}}{\mathrm{d}t}x = f(t,x,u) = \begin{cases} A_0 x + B_0 u, & \text{if } t \in [0, dT_s], \\ A_1 x + B_1 u, & \text{if } t \in [dT_s, T_s], \end{cases} \tag{2.58}$$

where, as in the previous section, x is the vector of state variables, and u is the input voltage. The state-space averaged model (2.24) can be written in a more general form as

$$\frac{\mathrm{d}}{\mathrm{d}t}\langle x\rangle = g\big(\langle x\rangle, u\big), \tag{2.59}$$

where $\langle x\rangle$ represents the local average of x and

$$\begin{aligned} g\big(\langle x\rangle, u\big) &\triangleq \frac{1}{T_s}\int_t^{t+T_s} f\big(t, \langle x\rangle, u\big)\,\mathrm{d}t \\ &= \big[dA_0 + (1-d)A_1\big]\langle x\rangle + \big[dB_0 + (1-d)B_1\big]u. \end{aligned} \tag{2.60}$$

The KBM algorithm places the averaging method in a geometric framework by considering a change of variables [4]

$$x(t) = \big\langle x(t)\big\rangle + \Psi_1\big(t, \big\langle x(t)\big\rangle\big), \tag{2.61}$$

where $x(t)$ and $\langle x(t)\rangle$ are the solutions to (2.58) and (2.60), respectively, and $\Psi_1(t, \langle x(t)\rangle)$ is the ripple correction term to be obtained using the following procedure:

1. Take the difference between (2.58) and (2.60) and compute its indefinite integral:

$$\gamma_1(t,y) = \int f(t,y,u) - g(y,u)\,\mathrm{d}t. \tag{2.62}$$

2. Compute the time-average of γ_1 over one switching cycle and remove it from γ_1:

$$\Psi_1(t,y) = \gamma_1(t,y) - \frac{1}{T_s}\int_0^{T_s} \gamma_1(\tau,y)\,\mathrm{d}\tau. \tag{2.63}$$

The estimated ripple function Ψ_1 is piecewise linear because function f is piecewise linear, and is called the first-order ripple estimate. Generally, more accurate estimations can be obtained by considering the following change of variables [4]

$$x(t) = \langle x(t) \rangle + \Psi_1\big(t, \langle x(t) \rangle\big) + \Psi_2\big(t, \langle x(t) \rangle\big) + \Psi_3\big(t, \langle x(t) \rangle\big) + \cdots, \tag{2.64}$$

where Ψ_i is called the ith-order ripple estimation which are ith-order polynomials in t and can be determined sequentially using a procedure similar to that outlined above.

The first-order (linear) ripple current functions for the three basic converter topologies are given below, where v_{in} is the input voltage, v_0 is the average of the output capacitor voltage, and T_s is the switching cycle:

$$\hat{i}_L(t) = \frac{v_{\text{in}}}{2L}(d-1)(dT_s - 2t), \tag{2.65}$$

$$\hat{i}_L(t) = \frac{\langle v_0 \rangle}{2L}(d-1)(dT_s - 2t), \tag{2.66}$$

$$\hat{i}_L(t) = \frac{v_{\text{in}} + \langle v_0 \rangle}{2L}(d-1)(dT_s - 2t) \tag{2.67}$$

for the buck, boost and buck–boost converters, respectively. These functions are valid for the interval when the switch is ON, that is, $t \in [0, dT_s]$. Similar expressions can be obtained for the OFF-interval of the switch and for other converter topologies.

2.4.3 Complete Averaged Models and Subharmonic Instability

As an example, consider again the boost DC–DC converter shown in Fig. 2.15b. The state-space averaged model of the converter can be written as follows when a resistive load is assumed:

$$\frac{\mathrm{d}}{\mathrm{d}t}\begin{pmatrix} \langle i_L \rangle \\ \langle v_0 \rangle \end{pmatrix} = \begin{pmatrix} 0 & \frac{d-1}{L} \\ \frac{1-d}{C} & -\frac{1}{CR} \end{pmatrix}\begin{pmatrix} \langle i_L \rangle \\ \langle v_0 \rangle \end{pmatrix} + \begin{pmatrix} \frac{v_{\text{in}}}{L} \\ 0 \end{pmatrix}. \tag{2.68}$$

The instantaneous inductor current at the switch turn-off instant can be written as $\langle i_L \rangle + \hat{i}_L(dT_s)$ so that the following duty ratio constraint is obtained:

$$i_p - m_c dT_s = \langle i_L \rangle + \hat{i}_L(dT_s). \tag{2.69}$$

Based on the first-order ripple current function (2.66), this can be more specifically written as

$$i_p - m_c dT_s = \langle i_L \rangle + \frac{dT_s(1-d)\langle v_0 \rangle}{2L}, \tag{2.70}$$

where the variables are as defined in Fig. 2.15b and Fig. 2.20. This combined with (2.68) defines a complete averaged model for boost converter under peak-current control.

The averaged model (2.68) and (2.70) can be used to study various characteristics of the converter. Of particular interest is the ability of the model to predict the subharmonic instability discussed in the previous subsection. Here we will examine this at three different levels: (a) the modulator gain, (b) the current loop gain, and (c) dynamics of the entire converter. In all cases, we will see that the averaged model can correctly predict the subharmonic instability [19].

The nonlinear duty ratio constraint (2.70) can be linearised to define a small-signal transfer function from the average inductor current to the duty ratio, as given below:

$$\frac{D(s)}{\langle I_L(s)\rangle} = \frac{1}{-[m_c + (1/2 - D)(M_1 + M_2)]T_s}. \tag{2.71}$$

This essentially defines the gain of the modulator from the inductor current to the duty ratio under peak-current control. Symbols in capital letters in the above equation (as well as throughout the rest of the section) represent steady-state values of the corresponding variables in lower cases. (For example, M_1 represents the steady-state value of m_1.) As can be seen, when no slope compensation is included (i.e. $m_c = 0$), the small-signal modulator gain (2.71) becomes positive when the steady-state duty ratio, D, exceeds 0.5. This corresponds to a current feedback control loop with a positive gain, hence indicating unstable operation.

To find the complete current loop gain, we note that the average model of the inductor current in a continuous conduction mode PWM converter can be written in general as

$$\frac{\mathrm{d}}{\mathrm{d}t}\langle i_L\rangle = dm_1 - (1-d)m_2.$$

Under the assumption that the converter input and output voltages are constant, the duty ratio to the average inductor current transfer function can be obtained from this model as

$$\frac{\langle I_L(s)\rangle}{D(s)} = \frac{M_1 + M_2}{s}. \tag{2.72}$$

Combining this with (2.71) yields the current loop gain of a boost converter under peak-current control:

$$I_c(s) = \frac{M_1 + M_2}{-[m_c + (1/2 - D)(M_1 + M_2)]T_s}\,\frac{1}{s}. \tag{2.73}$$

As can be seen, the loop gain is unstable for $D > 0.5$ when no slope compensation is used. This prediction is consistent with the sampled-data analysis results [26].

To examine the stability of the overall boost converter under peak-current control, note that the averaged model (2.68) is nonlinear but can be linearized around a given

operation point to give the following linear model:

$$\frac{\mathrm{d}}{\mathrm{d}t}\begin{pmatrix}\widehat{\langle i_L\rangle}\\ \widehat{\langle v_0\rangle}\end{pmatrix}=\begin{pmatrix}0 & \frac{D-1}{L}\\ \frac{1-D}{C} & -\frac{1}{CR}\end{pmatrix}\begin{pmatrix}\widehat{\langle i_L\rangle}\\ \widehat{\langle v_0\rangle}\end{pmatrix}+\frac{V_{\text{in}}}{1-D}\begin{pmatrix}\frac{1}{L}\\ -\frac{1}{CR(1-D)}\end{pmatrix}\hat{d}. \tag{2.74}$$

Meantime, linearisation of (2.70) gives the following small-signal duty-ratio constraint

$$\hat{d}=\frac{1-D}{V_x}\left[\begin{pmatrix}\frac{2L}{T_s}\\ D(D-1)\end{pmatrix}^{\top}\begin{pmatrix}\widehat{\langle i_L\rangle}\\ \widehat{\langle v_0\rangle}\end{pmatrix}+\frac{2L}{T_s}\hat{i}_p\right],$$

where $V_x=2(D-1)Lm_c+(2D-1)V_{\text{in}}$. A complete small-signal model of the converter is obtained by substituting the above expression into (2.74). The system matrix of the combined small-signal model is found to be

$$A=\begin{pmatrix}0 & \frac{D-1}{L}\\ \frac{1-D}{C} & -\frac{1}{CR}\end{pmatrix}+\frac{V_{\text{in}}}{V_x}\begin{pmatrix}\frac{2}{T_s} & \frac{D(D-1)}{L}\\ -\frac{2L}{RCT_s(1-D)} & \frac{D}{CR}\end{pmatrix}. \tag{2.75}$$

Stability of the converter depends on the eigenvalues of A, that is, the roots of the characteristic polynomial $\det(sI-A)$. In the case when no slope compensation is used, A can be written as

$$A=\begin{pmatrix}\frac{2}{T_s}\ \frac{1}{2D-1} & \frac{D-1}{L}\ \frac{3D-1}{2D-1}\\ \frac{1-D}{C}-\frac{2L}{RCT_s(1-D)(2D-1)} & \frac{1}{CR}\ \frac{1-D}{2D-1}\end{pmatrix}. \tag{2.76}$$

Hence

$$\det(sI-A)=s^2+\frac{s}{1-2D}\left(\frac{2}{T_s}+\frac{1-D}{RC}\right)+a_0. \tag{2.77}$$

Note that the coefficient of s in (2.77) is negative when $D>0.5$, in which case at least one root of the characteristic polynomial will be positive because the sum of the two roots is equal to the inverse of this coefficient. This confirms again the ability of (2.70) as the duty-ratio constraint to predict subharmonic instability under peak-current control.

2.5 Summary

Pulse-width modulation is the foundation of control in power electronics. Among various modulation methods, constant-frequency PWM using a sawtooth or triangle carrier is most common in practice. When the reference is a sine wave, the use of a triangle carrier has an additional benefit that odd-order sideband components of

odd-order carrier harmonics as well as even-order sideband components of even-order carrier harmonics are eliminated. Closed-form spectral models developed using double Fourier analysis facilitated the analysis and comparison of these PWM methods.

The pulse-width modulator is also an integral part of the feedback control loop and needs to be properly modelled for control design. A constant-frequency modulator can be modelled by a constant gain, but such linear time-invariant model is only valid up to half the carrier frequency. Beyond this frequency, the modulator response to a perturbation in the reference may be affected by sideband components of the perturbation (when the perturbation frequency is a multiple of one half of the carrier frequency) and cannot be modelled by a constant gain. A variable-frequency modulator can also be modelled by a DC gain with a leading phase. The DC gain changes with the ON and OFF time, but the variation is small and can be ignored in practice. The leading phase adds to the phase margin of the control loop and is beneficial for control stability.

Multiple PWM converters can be connected in parallel or in series to form a modular design with scalable current or voltage capacities. In such modular systems, interleaving offers an opportunity to reduce the combined input or output harmonics through harmonic cancellation among different modules. The traditional symmetric interleaving method eliminates all but N-multiples of the carrier harmonic for N modules connected in parallel or in series. Additionally, the harmonic cancellation effect is such that, when a carrier harmonic is eliminated, all of its sideband harmonics are eliminated as well. Asymmetric interleaving makes it possible to selectively reduce different carrier harmonics and their sideband components to achieve different objectives, such as minimisation of EMI filter size.

Peak-current control is a special form of control in which there is no explicit PWM process. The current ripple is effectively used as a carrier signal in an equivalent PWM process. Averaged models can be used to study both steady-state and dynamic characteristics, including ripple instability, of peak-current controlled converters. A key step in the development of such averaged model is a duty ratio constraint that models the equivalent PWM process. Duty ratio constraints developed based on ripple estimation using the KBM method are provided for commonly used converters and are shown to correctly predict the ripple instability.

References

1. Beechner, T., Sun, J.: Asymmetric interleaving—a new approach to operating parallel converters. In: Proc. of the IEEE Energy Conversion Congress and Exposition, San Jose, California, USA, pp. 99–105 (2009)
2. Bennett, W.R.: New results in the calculation of modulation products. Bell Syst. Tech. J. **12**(4), 238–243 (1933)
3. Black, H.S.: Modulation Theory. Van Nostrand Reihnold, New York (1953)
4. Bogoliubov, N.N., Mitropolsky, Y.A.: Asymptotic Methods in the Theory of Nonlinear Oscillations. Hindustan Publishing Corporation, New Delhi (1961)
5. Bowes, S.R., Bird, B.M.: Novel approach to the analysis and synthesis of modulation processes in power convertors. IEE Proc. **122**(5), 507–513 (1975)

6. Cuk, S., Middlebrook, R.D.: A general unified approach to modeling switching power stages. In: Proc. of the IEEE Power Electronics Specialists Conference, Cleveland, Ohio, USA, pp. 18–31 (1976)
7. Dixon, L.H.: Average Current-Mode Control of Switching Power Supplies. Unitrode Power Supply Design Seminar Handbook, Merrimack, New Hampshire, USA (1990)
8. Erickson, R.W., Maksimovic, D.: Fundamentals of Power Electronics, 2nd edn. Kluwer Academic Publishers, Dordrecht (2001)
9. Holmes, D.G., Lipo, T.A.: Pulse Width Modulation for Power Converters—Principles and Practice, 1st edn. Wiley–IEEE Press, Piscataway (2003)
10. Hsu, S.P., Brown, A., Rensink, L., Middlebrook, R.D.: Modeling and analysis of switching dc-to-dc converters in constant-frequency current-programmed mode. In: Proc. of the IEEE Power Electronics Specialists Conference, San Diego, California, USA, pp. 284–301 (1979)
11. Maksimovic, D., Jang, Y., Erickson, R.: Nonlinear-carrier control for high-power-factor boost rectifiers. IEEE Trans. Power Electron. **11**(4), 578–584 (1996)
12. Ridley, R.B.: A new, continuous-time model for current-mode control. IEEE Trans. Power Electron. **6**(2), 271–280 (1991)
13. Sanchez, M., Popert, F.: Uber die Berechrung der Spektren modulierter Impulsfolgen. Arch. Elecktr. Ubertrag. **9**(10), 441–452 (1955)
14. Sun, J.: Small-signal modeling of variable-frequency pulse-width modulators. IEEE Trans. Aerosp. Electron. Syst. **38**(3), 1104–1108 (2002)
15. Sun, J.: Modeling and analysis of pulse-width modulation. In: Professional Education Seminar at IEEE Applied Power Electronics Conference, Austin, Texas, USA (2008)
16. Sun, J., Bass, R.M.: Automated ripple analysis of PWM DC/DC converters using the KBM method. In: Proc. of the IEEE International Conference on Industrial Electronics, Control, and Instrumentations, Atlanta, Georgia, USA, pp. 621–626 (1997)
17. Sun, J., Bass, R.M.: A new approach to averaged modeling of current-programmed PWM converters. In: Proc. of the IEEE International Conference on Industrial Electronics, Control, and Instrumentation, New Orleans, Louisiana, USA, pp. 599–604 (1997)
18. Sun, J., Chen, M.: Nonlinear average current control using partial current measurement. IEEE Trans. Power Electron. **23**(4), 1641–1648 (2008)
19. Sun, J., Choi, B.: Averaged modeling and switching instability prediction for peak current control. In: Proc. of the IEEE Power Electronics Specialists Conference, Recife, Brazil, pp. 2764–2770 (2005)
20. Sun, J., Grotstollen, H.: Optimal space vector modulation and regular-sampled PWM: a reexamination. In: Proc. of the IEEE Industry Applications Society Annual Meeting, San Diego, California, USA, pp. 956–963 (1996)
21. Sun, J., Grotstollen, H.: Symbolic analysis methods for averaged modeling of switching power converters. IEEE Trans. Power Electron. **12**(3), 537–546 (1997)
22. Sun, J., Fröhleke, N., Grotstollen, H.: Harmonic reduction techniques for single-switch three-phase boost rectifiers. In: Proc. of the IEEE Industry Applications Society Annual Meeting, San Diego, California, USA, pp. 1225–1232 (1996)
23. Sun, J., Mitchell, D.M., Greuel, M., Krein, P.T., Bass, R.M.: Averaged modeling of PWM converters operating in discontinuous conduction mode. IEEE Trans. Power Electron. **6**(4), 482–492 (2001)
24. Tolstov, G.P.: Fourier Series. Prentice-Hall, Englewood Cliffs (1962)
25. UCC38501 BiCMOS PFC/PWM Combination Controller datasheet. Texas Instruments, Dallas, Texas, USA (1999)
26. Verghese, G.C., Bruzos, C.A., Mahabir, K.N.: Averaged and sampled-data models for current mode control: A reexamination. In: Proc. of the IEEE Power Electronics Specialists Conference, Milwaukee, Wisconsin, USA, pp. 484–491 (1989)

http://www.springer.com/978-1-4471-2884-7

Dynamics and Control of Switched Electronic Systems
Advanced Perspectives for Modeling, Simulation and Control of Power Converters
Vasca, F.; Iannelli, L. (Eds.)
2012, XIV, 494 p., Hardcover
ISBN: 978-1-4471-2884-7